Localized water reverberation phases and its impact on backprojection images

Han Yue[1], Jorge C. Castellanos[2] ⓘ, Chunquan Yu[2] ⓘ, Lingsen Meng[3] ⓘ, and Zhongwen Zhan[2] ⓘ

[1]Department of Geophysics, School of Earth and Space Sciences, Beijing University, Beijing, China, [2]Seismological Laboratory, Department of Earth and Planetary Sciences, Caltech, Pasadena, California, USA, [3]Department of Earth and Planetary Sciences, UCLA, Los Angeles, California, USA

Abstract Coherent radiators imaged by backprojections (BP) are commonly interpreted as part of the rupture process. Nevertheless, artifacts introduced by structure related phases are rarely discriminated from the rupture process. In this study, we use a calibration event to discriminate between rupture and structure effects. We reexamine the waveforms and BP images of the 2012 M_w 7.2 Indian Ocean earthquake and a calibration event (M_w 6.2). The P wave codas of both events present similar shape with characteristic period of approximately 10 s, which are backprojected as coherent radiators near the trench. S wave BP does not image energy radiation near the trench. We interpret those coda waves as localized water reverberation phases excited near the trench. We perform a 2-D waveform modeling using realistic bathymetry model and find that the steep near-trench bathymetry traps the acoustic water waves forming localized reverberation phases. These waves can be imaged as coherent near-trench radiators with similar features as that in the observations. We present a set of methodologies to discriminate between the rupture and propagation effects in BP images, which can serve as a criterion of subevent identification.

1. Introduction

Backprojection (BP) techniques are broadly used in imaging great earthquakes, yielding pictures of spatial-temporal evolution of kinematic ruptures. Energy bursts imaged by BP techniques are commonly identified as part of a continuous [*Ishii et al.*, 2005; *Xu et al.*, 2009; *Yagi et al.*, 2012; *Yao et al.*, 2013] or segmented ruptures process [*Meng et al.*, 2012; *Yue et al.*, 2012]. BP can also be used to identify early triggered aftershocks, short-term aftershocks, and local seismicity [*Fan and Shearer*, 2016a, 2016b; *Inbal et al.*, 2015; *Kiser and Ishii*, 2013], which detect substantial events missed in the catalog. Since earthquakes can be beamformed as coherent radiators in BP images, a reverse logic is commonly, but not rigorously, adopted to interpret coherent radiators as subevents or aftershocks. Nevertheless, other phases that are not directly related to a rupture process, e.g., scattered and focused/defocused phases, may also present spatial coherency and be misidentified as rupture processes. Analysis to discriminate between the structure and rupture related phases are rarely performed in BP result analysis, which lead to uncertainty in the event identification.

Most great earthquakes occur in the subduction zones beneath oceans. Reflected and reverberated water phases are often of substantial amplitude in their teleseismic P wave codas, which is not negligible in related waveform modeling and source inversion studies. *Wiens* [1989] investigated the bathymetry effect on body waves and demonstrated that the dipping bathymetry introduces significant water-phase complexity. *Okamoto and Takenaka* [2009] applied 2.5-D numerical modeling in finite source inversion and demonstrated that bathymetry effect is nonnegligible and smears the pattern of the slip distribution. *An et al.* [2017] adopted path calibration analysis in the 2015 Illapel earthquake study and indicated that prolonged P wave codas can be excited by near-trench ruptures. Inadequate modeling of those phases may produce artificially long source rupture [*Lee et al.*, 2016]. Most previous studies about water phases are related to the effect on earthquake modeling and inversion, and the effect on BP imaging studies is rarely discussed. In this study, we adopt waveform analysis, backprojection, and modeling techniques and use the 2012 M_w = 7.2 Indian Ocean strike-slip event as an example to demonstrate that localized water phase can generate strong coherent radiators and leads to misinterpretation of BP results.

1.1. The 2012 M_w = 7.2 Indian Ocean Earthquake

In 2012, a series of great earthquakes shocked the floor of the Indian Ocean, with a M_w 8.6 strike slip event preceded by a M_w 7.2 (10 January 2012) foreshock and followed by a M_w 8.2 aftershock (Figure 1) [*Duputel*
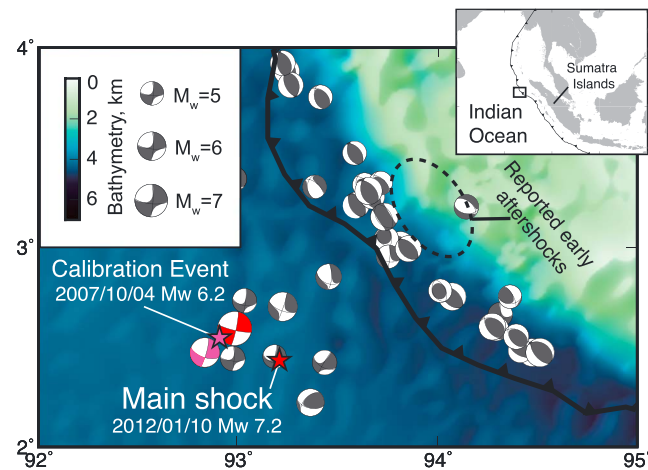
Figure 1. The GCMT solution of the 2012 $M_w = 7.2$ main shock and the 2007 $M_w = 6.2$ calibration event are plotted with red and magenta filled focal mechanisms, respectively. Their associated epicenter locations (PDE) are marked by red and magenta filled stars, respectively. Background seismicity (2005–2016) for $4.5 < M_w < 8.0$ earthquakes (GCMT catalog) are plotted with gray filled focal mechanisms. The trench line [*Bassett and Watts*, 2015] is plotted with a black barbed curve. The location of reported early triggered aftershocks [*Fan and Shearer*, 2016a] are marked by a dashed ellipse. An insert map is plotted on the top right with the study area marked with a rectangle.

et al., 2012; *Hill et al.*, 2015; *Meng et al.*, 2012; *Wei et al.*, 2013; *Yue et al.*, 2012]. The regional seismicity can be grouped as thrusting events located near the subduction zone and strike-slip events located seaward of the trench (Figure 1). *Fan and Shearer* [2016a] applied backprojection technique to the $M_w = 7.2$ event and imaged coherent sources near the trench, close to a cluster of background seismicity (Figure 1). These coherent radiators were attributed to a series of early dynamically triggered aftershocks. As discussed above, the early triggered sequence can be misidentified from propagation effects. To discriminate between the source and propagation effects, we selected a $M_w = 6.2$ earthquake (4 October 2007) as a reference event to calibrate the propagation effect (Figure 1). For simplicity, from this point we call the $M_w = 7.2$ event as the main shock and the $M_w = 6.2$ event as the calibration event.

We assume a logic that is commonly used in empirical Green's function analysis: because the main shock and calibration event shares similar raypaths, similar patterns identified in both the main shock and calibration waveforms are attributed to the propagation effect; waveform and BP image discrepancies are attributed to differences in the rupture process, e.g., source duration and early triggered aftershocks. Waveform comparison between these two events can discriminate between the propagation and the source effect.

2. Waveform Analysis

From the Global Seismographic Networks (GSN), we selected 71 stations, by which both the main shock and calibration P waves are clearly recorded. The stations are selected to ensure a good azimuth coverage. Waveforms are aligned at the calibration P wave initial arrival using a Matlab GUI-based package (CrazySeismic [*Yu et al.*, 2017]). P waves of both the main shock and calibration waveforms are band-passed filtered with corner frequencies at 0.02 and 0.5 Hz. As shown in Figure 2, at least four phases with sinusoidal moveout can be identified in both the main shock and calibration waveforms. Those phases present similar shapes and generally constant intervals, which indicate they are generated within a compact area with recurrence time of approximately 10 s. Assuming those radiators are point sources, we invert for their loci with the arrival time of peaks. Details of the relocation technique are described in the supporting information. For both the main shock and the calibration event, the coherent sources are relocated near the trench within a compact area (Figure 3). Figure 2 shows the arrival time of those peaks are well predicted by these coherent sources with interval of 10–12 s. Both the main shock and calibration event present similar coda, which indicates the codas are associated with the propagation effect. We plotted the tangential component of the main shock SH waves recorded at 64 global teleseismic stations (Figure 2c). No clear sinusoidal waveforms are identified in the S wave codas, which indicates that the SH waves are not efficiently radiated from those radiators. We perform the same waveform analysis and BP techniques to another calibration event, and similar features are also resolved for that event (Figure S1).

2.1. Temporal-Spectral Analysis

With temporal-spectral analysis, we can identify the resonance frequency of particular waveform segments [*An et al.*, 2017; *Ihmlé and Madariaga*, 1996]. Examples of teleseismic P waves of both the main shock and calibration event are plotted in Figure 4. For both events, the initial 50 s is characterized with a source spectrum
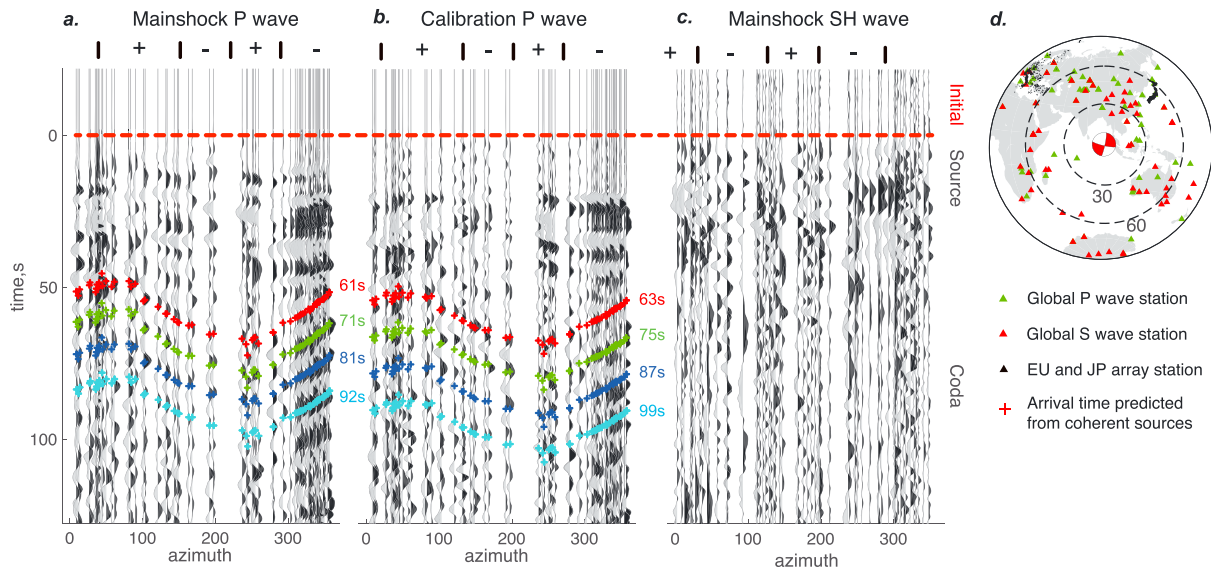
Figure 2. (a) Teleseismic *P* waves of the main shock are aligned at 0 s (red dashed line) and sorted by azimuth. Predicted arrival times from the coherent radiators are marked with color-coded "+." The same colors are used to mark the inverted point source locations in Figure 3a. The *P* wave polarities are calculated from the main shock focal mechanism and marked above the waveforms. (b) The same as Figure 2a but for teleseismic *P* waves of the calibration event. (c) The same as Figure 2a but for teleseismic SH waves of the main shock. (d) Stations recording teleseismic *P* and *S* waves are marked with green and red filled triangles, respectively. European and Japanese (F-net) network stations, used for array backprojections, are plotted with black filled triangles.

[*Brune*, 1970] that the spectrum is flat at low frequency and drops beyond the corner frequency. The spectra of the *P* wave codas (after 50 s) present a characteristic frequency peaked around 0.1 Hz, which appears to be a nonearthquake signal. A flat water layer with thickness of 3.75 km generates resonance period of 10 s [*An et al.*, 2017], assuming 1.5 km/s *P* wave velocity in water. Depth contour of 3.75 km cuts close to the near trench radiators (Figure 3), and the associated resonance frequency is consistent with the recurrence intervals of those radiators (10–12 s). The resonance frequency shows slight change over time which may reflect lateral migration of reverberation waves in a nonflat water layer. The trench area presents significant bathymetry
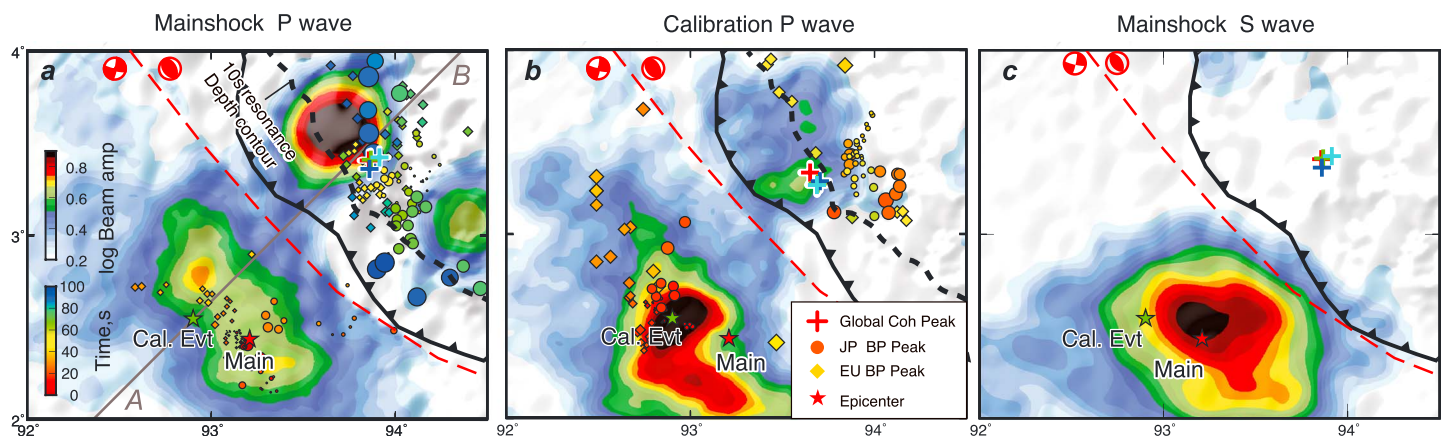

Figure 3. (a) Time-integrated *P* wave beam amplitude is plotted with a white-black color scale as the background map. Epicenter locations of the main shock and calibration event are marked with red and green filled stars. Coherent radiators are marked with color-coded +. The same colors are used to mark the associated predicted arrival times in Figure 2a. The focal mechanisms used to calculate the stacking polarity are indicated with red filled beach balls in two domains with the boundary indicated by a red dashed curve. HF radiators imaged by European and Japanese arrays are marked with color coded diamonds and circles, respectively. The imaging time are indicated by their filling color. The trench is marked by a black barbed curve. The bathymetry counter (along 3.75 km depth) are plotted with a black dashed curve. The profile AB is marked as a gray line, which is used to cut the bathymetry profile for modeling and interpolate 1-D BP image in Figure 5. (b) The same as Figure 3a but for the calibration event. (c) The same as 3a but for the BP of main shock SH wave.
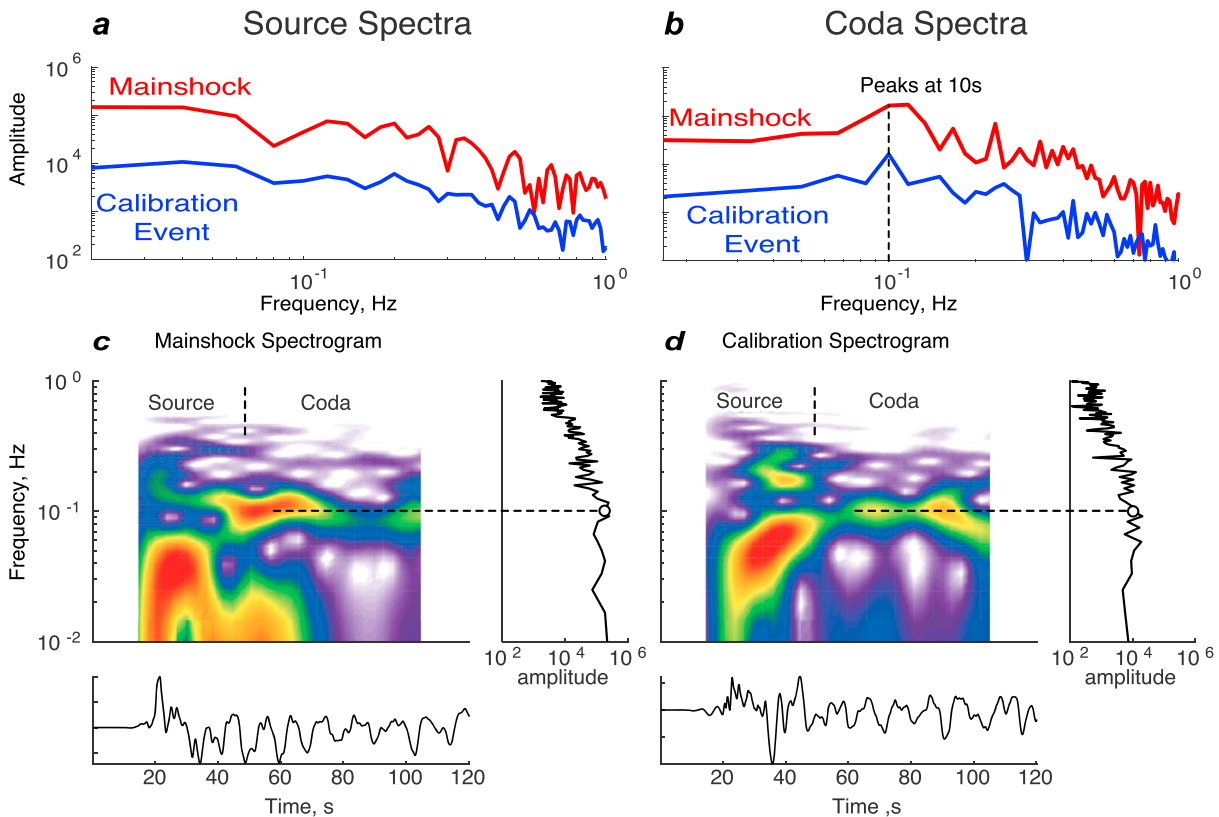
Figure 4. (a) Spectra of the source waveforms (0–50 s at station BJT) of the main shock and calibration event are plotted in red and blue, respectively. (b) Spectra of the codas (50–100 s at station BJT) of the main shock and calibration event are plotted in red and blue curves, respectively. (c and d) Spectrogram of the main shock and calibration teleseismic *P* waves recorded at station BJT are plotted in Figures 4a and 4b, respectively. For each subplot, the waveforms are plotted in the bottom panel, and the spectrum are plotted in the right panel. Spectra associated with the source and reverberation phases are separated by a black dashed line.

slopes that its resonance feature cannot be completely explained by 1-D water layer resonance; however, the first-order consistency between the 1-D layer prediction and the observations indicates that the observed *P* wave coda can be interpreted as water reverberation phases.

3. Backprojection

To test if the identified phases can be beamformed as coherent radiators, we backproject the teleseismic *P* waves of both the main shock and the calibration event to the source region. We adopted a fourth-order root stacking technique using global *P* wave recordings [*Xu et al.*, 2009]. We use the same band-pass filter as described in the last session; thus, relatively low frequency (0.01–0.2 Hz) energy are stacked by this technique. Details of BP techniques are described in the supporting information. In both the main shock and calibration BP results, two areas with high time-integrated beam amplitude are imaged near the epicenters and the trench, respectively. The near-trench radiator is close to the relocated point sources (Figure 3). The near-trench radiator of the main shock presents a stronger stacked beam amplitude than that near the epicenter, which is also shifted (~15 km) to the SW from the relocated point sources; these effects are not observed in the calibration BP results. The calibration BP image presents two peaks near the trench and the northern one colocates with the peak of the main shock. It indicates that two localized radiators may exist near the trench and the northern one is more efficiently excited by the main shock. The rupture directivity, source duration, and hypocentral depths are different between the main shock and the calibration event, which may lead to different excitation amplitude to the near-trench radiators. The first-order consistency between the main shock and calibration BP images demonstrates that the coherent sources near the trench are introduced by the propagation effect. The same backprojection technique is adopted to teleseismic SH waves and plotted in Figure 3c. Strong integrated beam amplitude is only imaged near the epicenter indicating those

near-trench radiators do not radiate SH waves. Similar waveform analysis and BP technique are adopted to another calibration event, and similar features are found in those results (Figure S1).

Regional array-based BP are performed using European and Japanese (F-net) array recordings. We adopted a band-pass filter with higher corner frequency (0.1–2 Hz); thus, relatively high frequency (HF) energy is imaged in the array BP technique. A MUSIC (Multiple Signal Classification) BP technique [*Meng et al.*, 2011] is adopted to the array data. The detailed BP techniques are described in the supporting information. Radiators near the epicenter and the trench region are both observed in the array HF BP images (Figure 3). The near-trench radiators appear to be excited after 30 s and are most significant after 60 s, which is consistent with the *P* and *S* wave arrivals at trench. This phenomenon is also revealed in the animated global BP results (Movies S1 and S2).

4. 2-D Simulation

The phases related to the near-trench radiator present resonance frequency in consistency with water reverberation phases and are evident only in *P* wave codas. We attribute the near-trench radiators as a result of localized water *P* wave reverberations; thus, the geometry of the ocean floor appears to be the key attribute generating those phases. Meanwhile, both events excite such radiators in the trench normal projection; thus, the wavefield is approximately symmetric in the trench parallel direction. We assume that the first-order characteristic of the water reverberation phases can be modeled as a two-dimensional wave propagation problem along the trench normal direction. We perform a 2-D finite difference (FD) simulation [*Li et al.*, 2014] with a simplified two-domain (i.e., fluid and solid) velocity model to simulate the bathymetry effect. The bathymetry (boundary) profile is cut along the trench normal direction from ETOPO1 global relief model (https://www.ngdc.noaa.gov/mgg/global/global.html) along profile AB in Figure 3. This model captures the bathymetry effect while still keeps a relatively simple wavefield; thus, wavefronts can be clearly identified and calculated. Details of simulation and visualization techniques are described in supporting information.

The 2-D simulation is performed to validate if the water reverberation phases can be imaged as coherent radiators near the trench. BP technique assume point sources at each imaging point and stack waveforms over theoretical wavefronts, which are simply concentric circles in the simulated wavefield. Therefore, curved wavefronts can be beamformed as coherent radiators. Wavefield snapshots are plotted in Figure 5, which reveals water reverberation phases can be excited by both *S* and *P* waves showing wavefronts with different slopes in the water layer, i.e., pw_n and sw_n phases (Figure 5a). Here "n" denotes phases related to the n time water surface reflection. Water phases refracted at the flat ocean floor presents linear wavefront, which cannot be backprojected as coherent sources (Figure 5a). *P* waves are scattered from the bathymetry roughness throughout the ocean bottom and generate curved wavefronts. These waves can be imaged as coherent radiators which are significant in HF BP images (Figure S3). Water phases reflected and refracted near the trench are modified with curved wavefronts, i.e., pw_2 and pw_1P (Figure 5b). After second reflection near the trench, wavefront is modified to vertical propagation, which forms a standing wave near the trench (pw_3 in Figure 5c). This explains why localized radiators are trapped near the trench. The water reverberations are also evident in the sw_n wavefield, which emit sw_nP phases showing in *P* wave codas (Figure S2).

To verify if the 2-D synthetics can be beamformed as coherent radiators, we perform a 1-D backprojection using waveforms recorded at 700 km depth. The beamforming technique used in the synthetic data is the same as that used in global BP (Figure 5e). We interpolate the global BP image along profile AB (Figure 3), which converts the observational 2-D BP image to 1-D cross sections. Both observed and synthetic 1-D BP images are visualized in the distance versus time domain in Figures 5d and 5e for comparison. As shown clearly by such comparison, the time-integrated beam amplitude of both images present a peak near the trench. Those are associated with a chain of radiators excited near the trench between 20 and 70 s. Both images show that the radiators are excited after *P* wave arrival and most significantly after *S* wave arrival, indicating an efficient *S* wave excitation. Near-trench radiators of both images present peak interval of ~5 s associated with the amplitude of both peaks and troughs, which is consistent with a resonance frequency of ~10 s. The 2-D modeling recover the main features shown in the observational BP images, with the bathymetry geometry as the only nonhomogeneous attribute in the velocity model. This indicates that the bathymetry is the key factor generating the near-trench coherent radiators and dynamically triggered aftershocks are not required to produce those radiators. BP is also performed with HF synthetic waveforms, which presents
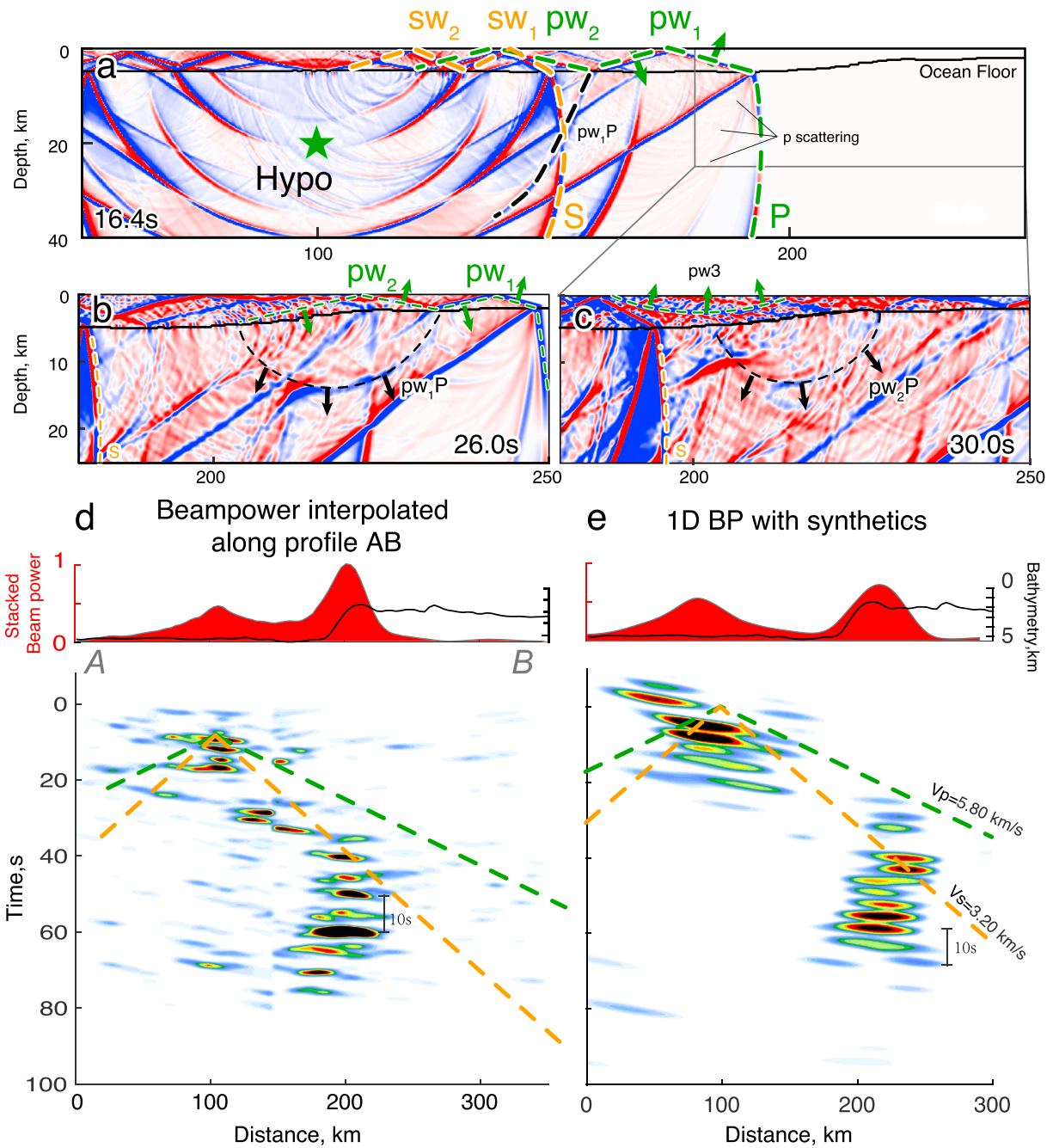
Figure 5. (a–c) Snapshots of 2-D wavefield (vertical displacement) are imaged at different time shots. (a) A 16.4 s wavefield snapshot near the source region. The wavefield is imaged with a red-blue color scale. The ocean floor is plotted as a black curve. The hypocenter is marked with a green filled star. The initial P and S wavefronts are marked with green and orange dashed curves, respectively. Secondary phases are labeled, including the scattered P waves, water reverberations, and refracted water waves (pw_1P). (b and c) Wavefield snapshots at 26 and 30 s near the trench area. Curved wavefronts generated by refracted and reflected water phases near the trench (pw_1P, pw_2P, and pw_3) are labeled. The plotting area is marked as a black box in Figure 5a. (d) The 1-D beam amplitude profile interpolated along profile AB (Figure 3a) from the main shock global BP image. Time-integrated beam amplitude is plotted in red in the top panel, with the associated bathymetry profile plotted as a black curve. Time versus distance image of the log beam amplitude is imaged with a white-black color scale in the bottom panel. Wavefronts calculated by 5.8 km/s and 3.2 km/s wave velocity is marked as green and orange dashed lines, respectively. (e) The same as Figure 5d but plotted for the 1-D BP image using synthetic data.

higher beam amplitude at small-scale bathymetry structures indicating that HF BP is more sensitive to small-scale bathymetry structures. This may be related to the discrepancy between the observed HF and LF BP images, which the HF BP image presents broadly distributed radiators in the trench area.

The 2-D modeling is performed to understand how localized water phases are generated, which demonstrates the interaction between wavefront and bathymetry gradient produce point radiators within the trench normal plane (modeling plane). Meanwhile, the tangential point is the first and only point when the wavefront reach the trench, which produce point sources in the trench parallel direction. Therefore, the coherent radiators in the 2-D modeling are also point sources in 3-D, which produce azimuth dependent moveout (Figure 2). The BP of 2-D synthetics recovered the main features of the near-trench radiators, e.g., time interval, initial/end time, and locations, which demonstrates the excitation mechanism of localized water reverberation phases. To fully recover the details of observed BP images, 3-D modeling with a realistic velocity structure and real station distributions are required. Sedimentary layers near trench can amplify the coda waves [*Okamoto*, 1993], as also influence the transmission between the liquid and solid layers. The 2-D modeling cannot capture such effects nor 3-D geometric spreading; thus, the beam amplitude of the synthetic test is not discussed. Detailed comparison with 3-D synthetics needs to be performed and discussed in more detailed studies.

5. Discussion and Conclusion

In this study, we applied waveform analysis and BP imaging technique to both the 2012 M_w 7.2 earthquake and a M_w 6.2 calibration event. We detect similar P wave codas at 10 s characteristic period in both events, with similar shapes and time intervals. Those phases are beamformed as coherent radiators near the trench. We adopt the logic of path calibration and attribute those phases as structure effects and interpret these phases as localized water reverberation phases. We performed 2-D synthetic tests with realistic bathymetry model, which demonstrates that the bathymetry slope distorts the wavefront and produces localized water reverberation phases. Backprojection with the synthetic waveforms produce coherent radiators near the trench, similar to those observed in the BP images of real observations. Ringing P waves was initially discovered and discussed by *Ward* [1979]. Localized water reverberation phases excited by megathrust earthquakes were reported by *An et al.* [2017] and *Ihmlé and Madariaga* [1996]. *An et al.* [2017] demonstrate that such phases are more efficiently excited by near-trench ruptures. *Ihmlé and Madariaga* [1996] used spectrogram and slant stack techniques to analyze the P wave codas of the 1995 Chile $M_w = 8.1$ event and 1994 Kurile Island $M_w = 8.3$ event. They attribute the monochromatic P wave codas (14 s period) to localized water reverberation phases, which is identical to the conclusion of this study.

BP technique provides first order estimation of rupture process and from this perspective it is valid in great earthquake studies. However, when interpreting secondary features in the BP images, discrimination between source and propagation effects needs to be made. As demonstrated in this study coherent radiators can be generated from near-trench reverberation phases and ocean bottom scattering. From a global perspective, trench areas commonly present substantial curvatures in bathymetry, thus, it may be a common effect that an underocean earthquake can excite localized water reverberation phases. Particularly but not exclusively, for events seaward of the trench, such discrimination needs to be performed. For example, *Fan and Shearer* [2016b] reported that normal events ($M_w > 7$) seaward of the trench appear to have 76.9% triggering rate near the trench, indicating that coherent radiators are broadly observed. This study provides a strategy to discriminate between structure and source-related signals using spectrogram analysis and path calibration techniques, which can serve as criteria of discrimination. Other propagation effects, e.g., structure scattering and focusing effect, may also generate such coherent radiators ,and their effect needs to be discussed in future studies.

References

An, C., H. Yue, J. Sun, L. Meng, and J. C. Baez (2017), The 2015 Illapel Chile (M_w=8.3) earthquake: Direction-reversed along-dip rupture with localized water reverberation, *Bull. Seismol. Soc. Am.*, *107*(5), doi: 10.1785/0120160393.

Bassett, D., and A. B. Watts (2015), Gravity anomalies, crustal structure, and seismicity at subduction zones: 1. Seafloor roughness and subducting relief, *Geochem. Geophys. Geosyst.*, *16*, 1508–1540, doi:10.1002/2014GC005684.

Brune, J. N. (1970), Tectonic stress and the spectra of seismic shear waves from earthquakes, *J. Geophys. Res.*, *75*(26), 4997–5009.

Duputel, Z., H. Kanamori, V. C. Tsai, L. Rivera, L. Meng, J.-P. Ampuero, and J. M. Stock (2012), The 2012 Sumatra great earthquake sequence, *Earth Planet. Sci. Lett.*, *351*, 247–257.

Fan, W., and P. M. Shearer (2016a), Fault interactions and triggering during the 10 January 2012 M_w 7.2 Sumatra earthquake, *Geophys. Res. Lett.*, *43*, 1934–1942, doi:10.1002/2016GL067785.

Fan, W., and P. M. Shearer (2016b), Local near instantaneously dynamically triggered aftershocks of large earthquakes, *Science*, *353*(6304), 1133–1136.

Hill, E. M., H. Yue, S. Barbot, T. Lay, P. Tapponnier, I. Hermawan, J. Hubbard, P. Banerjee, L. Feng, and D. Natawidjaja (2015), The 2012 M_w 8.6 Wharton basin sequence: A cascade of great earthquakes generated by near-orthogonal, young, oceanic mantle faults, *J. Geophys. Res. Solid Earth*, *120*, 3723–3747, doi:10.1002/2014JB011703.

Ihmlé, P. F., and R. Madariaga (1996), Monochromatic body waves zone earthquakes, *Geophys. Res. Lett.*, *23*(21), 2999–3002.

Inbal, A., R. W. Clayton, and J. P. Ampuero (2015), Imaging widespread seismicity at midlower crustal depths beneath Long Beach, CA, with a dense seismic array: Evidence for a depth-dependent earthquake size distribution, *Geophys. Res. Lett.*, *42*, 6314–6323, doi:10.1002/2015GL064942.

Ishii, M., P. M. Shearer, H. Houston, and J. E. Vidale (2005), Extent, duration and speed of the 2004 Sumatra–Andaman earthquake imaged by the Hi-Net array, *Nature*, *435*(7044), 933–936.

Kiser, E., and M. Ishii (2013), Hidden aftershocks of the 2011 M_w 9.0 Tohoku, Japan earthquake imaged with the backprojection method, *J. Geophys. Res. Solid Earth*, *118*, 5564–5576, doi:10.1002/2013JB010158.

Lee, S. J., T. Y. Yeh, T. C. Lin, Y. Y. Lin, T. R. A. Song, and B. S. Huang (2016), Two-stage composite megathrust rupture of the 2015 M_w8. 4 Illapel, Chile, earthquake identified by spectral-element inversion of teleseismic waves, *Geophys. Res. Lett.*, *43*, 4979–4985, doi:10.1002/2016GL068843.

Li, D., D. Helmberger, R. W. Clayton, and D. Sun (2014), Global synthetic seismograms using a 2-D finite-difference method, *Geophys. J. Int.*, *197*(2), 1166–1183.

Meng, L., A. Inbal, and J. P. Ampuero (2011), A window into the complexity of the dynamic rupture of the 2011 M_w 9 Tohoku-Oki earthquake, *Geophys. Res. Lett.*, *38*, L00G07, doi:10.1029/2011GL048118.

Meng, L., J.-P. Ampuero, J. Stock, Z. Duputel, Y. Luo, and V. Tsai (2012), Earthquake in a maze: Compressional rupture branching during the 2012 M_w 8.6 Sumatra earthquake, *Science*, *337*(6095), 724–726.

Okamoto, T. (1993), Effects of sedimentary structure and bathymetry near the source on teleseismic P waveforms from shallow subduction zone earthquakes, *Geophys. J. Int.*, *112*(3), 471–480.

Okamoto, T., and H. Takenaka (2009), Waveform inversion for slip distribution of the 2006 Java tsunami earthquake by using 2.5 D finite-difference Green's function, *Earth Planets Space*, *61*(5), e17–e20.

Ward, S. N. (1979), Ringing P waves and submarine faulting, *J. Geophys. Res.*, *84*(B6), 3057–3062.

Wei, S., D. Helmberger, and J. P. Avouac (2013), Modeling the 2012 Wharton basin earthquakes off-Sumatra: Complete lithospheric failure, *J. Geophys. Res. Solid Earth*, *118*, 3592–3609, doi:10.1002/jgrb.50267.

Wiens, D. A. (1989), Bathymetric effects on body waveforms from shallow subduction zone earthquakes and application to seismic processes in the Kurile trench, *J. Geophys. Res.*, *94*(B3), 2955–2972.

Xu, Y., K. D. Koper, O. Sufri, L. Zhu, and A. R. Hutko (2009), Rupture imaging of the M_w 7.9 12 may 2008 Wenchuan earthquake from back projection of teleseismic P waves, *Geochem. Geophys. Geosyst.*, *10*, Q04006, doi:10.1029/2008GC002335.

Yagi, Y., A. Nakao, and A. Kasahara (2012), Smooth and rapid slip near the Japan trench during the 2011 Tohoku-oki earthquake revealed by a hybrid back-projection method, *Earth Planet. Sci. Lett.*, *355*, 94–101.

Yao, H., P. M. Shearer, and P. Gerstoft (2013), Compressive sensing of frequency-dependent seismic radiation from subduction zone megathrust ruptures, *Proc. Natl. Acad. Sci. U.S.A.*, *110*(12), 4512–4517.

Yu, C., Y. Zheng, and X. Shang (2017), Crazyseismic: A MATLAB GUI-based software package for passive seismic data preprocessing, *Seismol. Res. Lett.*, *88*(3), 410–415.

Yue, H., T. Lay, and K. D. Koper (2012), En echelon and orthogonal fault ruptures of the 11 April 2012 great intraplate earthquakes, *Nature*, *490*(7419), 245–249.